Hydride superconductor structures of LaH_{10}, EuH_9, and UH_8 rationalized by electron counting and Jahn-Teller distortions in a covalent cluster model

Harry W. T. Morgan* and Anastassia N. Alexandrova

Department of Chemistry and Biochemistry, University of California, Los Angeles, Los Angeles, California 90095-1569, United States

E-mail: harrywtmorgan@g.ucla.edu

Abstract

The superconducting hydrides LaH_{10}, EuH_9 and UH_8 are studied using chemically intuitive bonding analysis of periodic and molecular models. We find trends in the crystallographic and electronic structures of the materials by focusing on chemically meaningful building blocks in the H sublattice. Atomic charge calculations, using two complementary techniques, allow us to assign oxidation states to the metals and divide the H sublattice into neutral and anionic components. Cubic $[H_8]^{q-}$ clusters are an important structural motif, and molecular orbital analysis of this cluster in isolation shows the crystal structures to be consistent with our oxidation state assignments. Crystal orbital hamilton population analysis confirms the applicability of the cluster model to the periodic electronic structure. A Jahn-Teller distortion predicted by MO analysis rationalises the distortion observed in EuH_9. Additionally, the performance of analytical methods at high pressures are tested and recommendations for future

studies are given. These results demonstrate the value of simple bonding models in rationalizing chemical structures under extreme conditions.

Introduction

Frenzied activity surrounds high-pressure hydrides due to reports of superconductivity near room temperature. In an effort to realise the prediction that hydrogen would become a room-temperature superconductor under sufficient pressure,[1] a variety of hydrogen-rich binary materials AH_x have been predicted and synthesized. Experimental milestones in this search include H_3S,[2] CaH_6,[3,4] LaH_{10},[5] and YH_9,[6] all of which exhibit critical temperatures above 200 K, and the retraction of a report of room-temperature superconductivity in an indeterminate compound of carbon, sulfur, and hydrogen.[7,8] This field has been driven by theoretical science from its inception, and many predictions of new hydride superconductors are yet to be realised. Indeed, the number of unverified predictions has drawn criticism from some researchers, including arguments against the BCS theory of superconductivity and questions over the validity of experimental evidence for superconductivity in hydrides.[9–11]

The "workhorse" of this field is crystal structure prediction (CSP), an umbrella term for computational methods for determining the crystal structure of a material without any prior information.[12–17] Studies utilizing this method generally identify the most thermodynamically stable phases for a chosen system (e.g. AH_x) as a function of pressure by running CSP calculations at various pressures and A:H ratios.[18] Superconducting critical temperatures can then be estimated for all candidate structures. However, our intuitive understanding of pressurized hydrides is underdeveloped, despite the large number of predictions made.

Nevertheless, some researchers have worked to understand these materials from a chemical perspective. "Chemical precompression" describes the strategy of 'alloying' hydrogen with another metal, so the compound should require less extreme pressures to induce superconductivity than would pure hydrogen.[13] A growing focus of material design is ternary

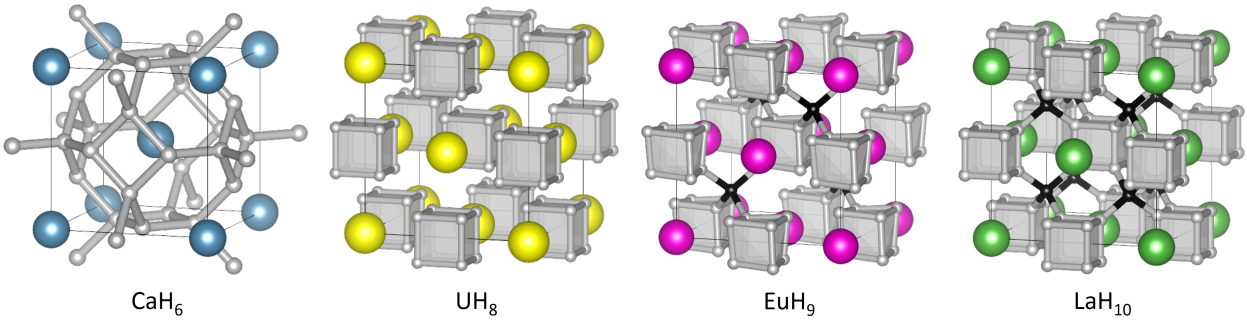

Figure 1: Structures of high-pressure hydrides CaH_6,UH_8, EuH_9, and LaH_{10}. In EuH_9 and LaH_{10}, grey and black spheres represent H atoms in cube and tetrahedral sites respectively.

hydrides ABH_x, where it is hoped that the combination of two metals will stabilize the phase at more accessible pressures due to additional chemical precompression.[19] The combinatorial space of ternary phases is much larger than the binary phases, so chemical insight must be combined with efficient computational procedures to search efficiently for candidate materials. Ion size effects have also been explored, as the reduction in enthalpy arising from dense packing of atoms is a major contributor to thermodynamic stability at high pressures. Some of the highly symmetrical binary hydride structures, such as CaH_6 and LaH_{10}, are the densest binary sphere packings (DBSPs) for the appropriate stoichiometry and radius ratio.[20,21] However, this model has major shortcomings; hard-sphere radii are poorly defined under pressure, particularly for hydrides, and it does not account for covalency in the anion sublattice. This may explain why many computed DBSPs have not been realised in any crystal structure.[21] Geometrical strain arising from size-cavity mismatch has been studied in a quantum chemical framework by chemical pressure density functional theory (CP-DFT), showing that distortions of symmetrical hydrides can indeed be caused by metal ion size (e.g. hexagonal channel widening in SrH_6 compared to CaH_6).[22,23] Chemical insight also led to the discovery of Eu_8H_{46}, a high-pressure hydride isostructural to the "Zintl clathrates" (e.g. Ba_8Si_{46}), because such large unit cells are too expensive to be included in routine CSP studies.[24]

The hydrogen sublattices in high-pressure hydrides are a mixed ionic/covalent system, and

can be viewed from several perspectives. The hard-sphere and CP-DFT approaches focus on the enthalpic stabilization of dense atomic packing, largely ignoring covalent effects. Many bonding studies focus on anion-cation interactions and the clathrate-like nature of the H sublattices, studying e.g. LaH_{32} as a cluster model of LaH_{10}, which may neglect important H-H covalent interactions.[25] Electron counting is widely used in solid state chemistry to assign formal oxidation states,[26] and can be used to rationalise structural trends through models like the Zintl-Klemm concept or the 18-n rule.[27,28] Solids containing cluster anions are particularly amenable to electron counting analysis - for example, the conductivities of metal hexaborides, MB_6, can be predicted from the metal valence state by application of the Wade-Mingos rules.[29–32] In this study we focus on covalent sub-units in the H-H networks of LaH_{10},[5] EuH_9,[24] and UH_8,[33,34] all shown in Figure 1, in order to explain structural trends. All three contain H_8 cubes in their anion sublattices, as shown in Figure 1, but the cubes are distorted in EuH_9, so we wish to explain the stability of this motif and the distortion in an electron counting framework. We analyse charge and bonding patterns in periodic structures, including benchmarking of analytical methods on CaH_6, and use these insights to devise cluster models which capture the balance of covalent and ionic behaviour of hydrogen. Crystal orbital hamilton population (COHP)[35,36] calculations validate the cluster models and reveal striking differences between inequivalent hydrogen atoms. Electron counting and molecular orbital theory provide intuitive explanations of structural differences between the hydrides.

Methodology

Periodic Density Functional Theory calculations were performed with VASP,[37] version 5.4.4, using the PAW[38]-PBE[39] method with plane-wave cutoff of 600 eV. k-point grids of 15-15-15 were used for optimizations of CaH_6, UH_8, and LaH_{10}, and a 12-12-12 grid was used for EuH_9. All geometries were optimized until the components of the forces on all atoms were

less than 0.03 eV/Å. Calculations on CaH_6 were performed using a hard H pseudopotential ("H_h") and a 700 eV plane-wave cutoff, though subsequent tests found that this did not cause a significant change to the structural optimizations compared to the ordinary H pseudopotential and a 600 eV cut-off (see Figure S1 for details).

Electron densities were analysed with the Quantum Theory of Atoms in Molecules (QTAIM) method.[40] Calculations were performed with the Bader program.[41] To ensure accurate results for compressed structures, we tested the effect of the number of points in the fine FFT grid along each lattice vector (NG(X,Y,Z)F in VASP) on the computed AIM charges for CaH_6. At 210 GPa, 200 points along each vector were required to ensure convergence of the Ca charges to within 0.05 $|e|$, while at ambient pressure this threshold is reached with the default value of 80. The H charges converged at 80 points at 0 GPa and 140 points at 0 GPa. Full results are available in Figure S2. In summary, in CaH_6 the metal charges converge with respect to FFT grid more slowly than the H charges, and pressure significantly increases the required number of grid points. All QTAIM results were collected with 250 grid points.

Local orbital bonding analysis was performed with LOBSTER.[42] Single-point calculations for LOBSTER analysis used 12-12-12 grids due to memory constraints. LOBSTER analysis requires projection of the plane-wave wavefunction into a local (Slater) orbital basis, and the quality of the results depends on the basis functions chosen for each element. Projection quality is measured by "charge spilling", which is the percentage of electron density lost by the projection. The dependence of charge spilling on basis set were determined for CaH_6, UH_8 and LaH_{10} by performing LOBSTER projections at various pressures with and without high-lying p orbitals ($4p$ for Ca, $6p$ for La, $7p$ for U). For all three compounds, the two bases give similar results at 0 GPa but inclusion of the extra p orbital causes the charge spilling to rise rapidly as pressure increases. In particular, for CaH_6 the larger projection basis gives a superior projection at 0 GPa (1.90% vs 2.34%) but much worse results at 210 GPa (10.4% vs 3.7%). Full results are available in Figure S3. Important conclusions from these tests:

1. Inclusion of diffuse, high-energy atomic orbitals worsens projection quality for com-

pressed structures

2. Basis sets must be tested on high-pressure structures

Full basis functions used in this study were Ca $3s3p4s$, La and Eu $4f5s5p5d6s$, U $5f6s6p6d7s$, H $1s$, with the PBEVaspFit basis set.[42] All projections for UH_8, EuH_9 and LaH_{10} have charge spillings of less than 3% except for UH_8 at 210 GPa (3.09%). 3% was recommended as a threshold for a good projection in a recent study on high-throughput analysis with LOBSTER.[43] COHP analysis of LaH_{10} and UH_8 was done with structures optimized at 0 GPa to maximise the quality of the projection.

Gas-phase DFT calculations were performed with ORCA,[44] version 5.0.3, using the PBE functional,[39] def2-SVP basis functions,[45] and a CPCM solvent model[46] with the dielectric constant of water to aid convergence of anions. The cubic H_8 structure was taken from the 150 GPa optimized structure of UH_8, and molecular orbitals were calculated by a single-point with a 6- charge. The distorted H_8 structure was taken from the 150 GPa optimized structure of EuH_9, and molecular orbitals were calculated by a single-point with a 2- charge.

Results and discussion

To establish a chemically intuitive picture of the metal hydrides, we optimized CaH_6, UH_8, EuH_9 and LaH_{10} at 0-210 GPa, in 30 GPa steps, and then calculated atomic charges with the aim of determining oxidation states for the metals. Results for EuH_9 could not be collected at 0-30 GPa because the H network optimized to form H_2 molecules, while the other phases were prevented from doing this by symmetry. Formal oxidation states are a valuable heuristic tool for assessing the electron distribution in a crystalline solid, particularly those with unusual anion networks. Calculations of atomic charges are conceptually challenging because they require the electron density shared between atoms to be partitioned. Here we use QTAIM,[40] based solely on electron density, and Mulliken analysis,[47] based on atomic orbitals, as the fundamentally different methods provide complementary pictures of the ma-

terials. Löwdin charges were also calculated, but gave correlations strongly at odds with the other two methods (Figure S4-6). Figure 2 shows the calculated charges of the metals from both methods.

All curves show that the magnitude of the metal charge decreases as pressure increases, be-

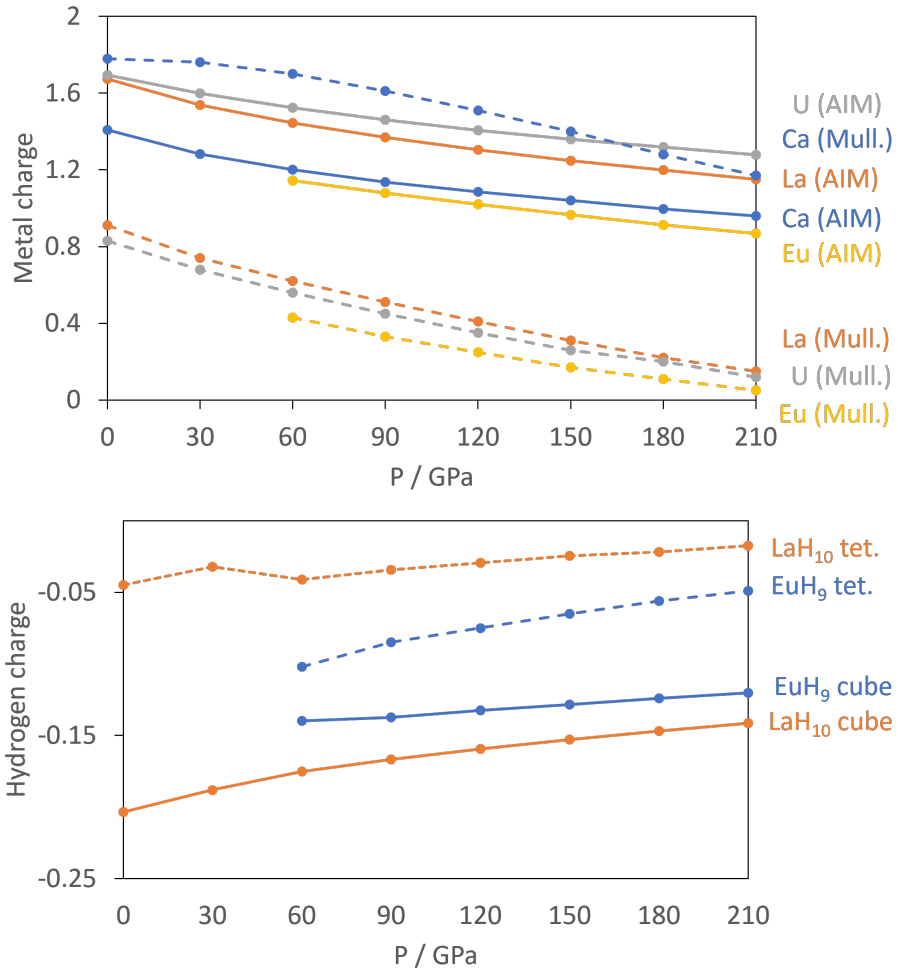

Figure 2: Upper: Computed charges of metal atoms in CaH_6 (blue), LaH_{10} (orange), UH_8 (grey) and EuH_9 (yellow) vs pressure. AIM charges are shown by solid lines, and Mulliken charges by dashed lines. Lower: AIM atomic H charges in EuH_9 (blue) and LaH_{10} (orange) resolved into cube (solid line) and tetrahedral (dashed line) atoms.

cause compression increases overlap and reduces charge separation. The AIM charges show small differences between the metals, with charges ranging from 1.4 to 1.8 at 0 GPa and increasing in the order Eu, Ca, La, U. The Mulliken charges have one qualitative difference in that Ca has a far larger charge - almost 2 - than the other three metals. This reflects

the strongly ionic nature of Ca, while Eu, La and U all have valence d orbitals which are low enough in energy to bond with the H network covalently. The computed charges are as expected in that Ca and Eu typically form +2 cations, La is typically 3+, and U can have oxidation states ranging from +3 to +6. Support for the assignment of Eu^{2+} comes from the spin moments of 6.81-6.82, indicative of a $4f^7$ configuration. The similarity between La and U in both methods suggests an assignment of U^{3+}, which would match UH_3, the ambient-pressure uranium hydride.

In the hydrogen charge calculations, the charges become less negative as pressure increases. For LaH_{10} and EuH_9 we can divide the hydrogens into those which form H_8 cubes, H^{cube}, and those which form the tetrahedral interstitial sites, H^{tet}. The two types are are shown as grey and black atoms respectively in Figure 1. The AIM hydrogen charges for EuH_9 and LaH_{10} are shown in Figure 2, separated into the cube and tetrahedral sites. Mulliken charges were excluded from the figure for clarity and can be found in Figure S8. The H^{tet} atoms have smaller negative charges than the H^{cube} atoms, according to both charge analysis methods, and resemble neutral atoms, while the H_8 cubes are anionic. For our electron-counting analysis of the H_8 cubes, we will therefore assume that the interstitial atoms are neutral and consider only electron transfer from the metal to H_8. This assumption allows us to treat UH_8, EuH_9 and LaH_{10} on an equal basis when rationalizing the symmetric and distorted cube geometries. The left-hand side of Figure 3 shows a molecular orbital (MO) diagram for a free H_8 cube, with O_h point symmetry, which is our starting point for studying the structures of UH_8, EuH_9 and LaH_{10}. The energetic ordering and shapes of the orbitals have been computed by DFT, but are shown here in a simplified representation - the computed orbitals and energies are shown in Figure S9.

Stable formal oxidation states arise from any configuration which gives completely filled valence shells. The simplest is neutral H_8, where the a_{1g} and t_{1u} sets are completely filled and the t_{2g} and a_{2u} sets are vacant, but this is not relevant to ionic materials. Completely filling the t_{2g} set gives a closed-shell H_8^{6-} ion, which fits into an extreme ionic counting

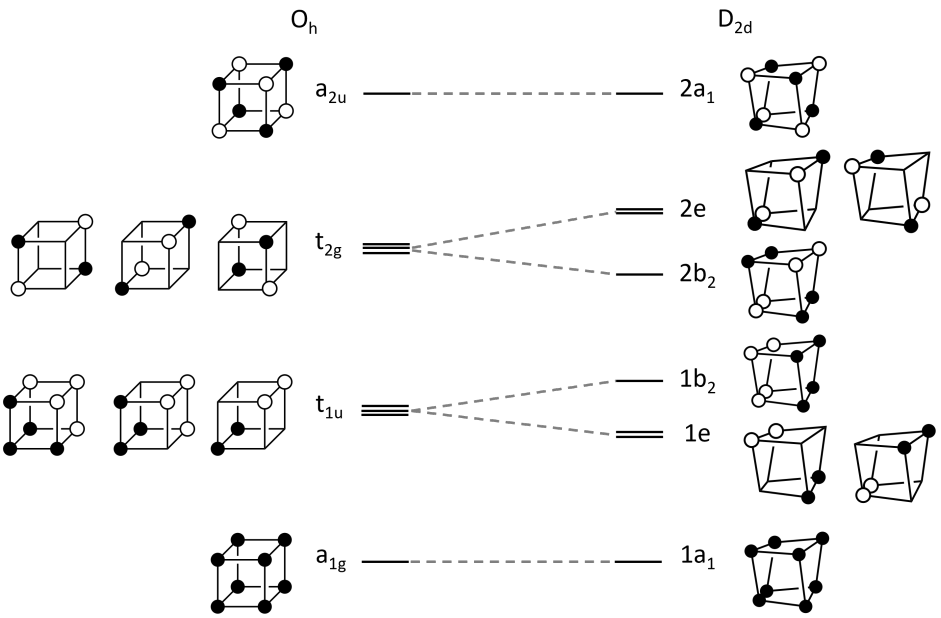

Figure 3: Walsh diagram showing orbital correlations between the cubic (O_h) and distorted (D_{2d}) geometries of an H_8 cluster.

picture of UH_8 since +6 is the highest accessible oxidation state for U. The final option is to singly fill the t_{2g} set, forming ${H_8}^{3-}$ which matches with La^{3+} in LaH_{10}, supporting the model of neutral tetrahedral H atoms. A free ${H_8}^{3-}$ ion would have a quartet ground state, having three unpaired electrons, but in a solid the spin information will be lost when the t_{2g} MOs form bands by overlapping with other atoms. The H-H bond lengths in the cubes offer another perspective on the oxidation state of U; the optimized cube edge length at 150 GPa in LaH_{10} is 1.231 Å, while in UH_8 it is elongated to 1.293 Å, consistent with additional electron donation into the antibonding t_{2g} orbitals. If a ${H_8}^{3-}$ charge is assigned to LaH_{10} then the bond lengths suggest that U is in an oxidation state higher than +3, *i.e.* +6. This extreme formal charge separation belies significant covalency between U and H_8.

To confirm the applicability of the molecular bonding model to the crystalline materials, we must show that hydrogen-metal interactions and H-H bonds between cube and tetrahedral atoms do not fundamentally change the bonding within the cube. We have therefore calculated crystal orbital hamilton populations (COHPs) for neighbouring pairs of atoms in LaH_{10}, which are shown in Figure 4. The plots on the left side of Figure 4 show COHPs for

a H^{cube}−H^{cube} bond and a H^{cube}−H^{int} bond. The principal peaks in the two COHP curves are non-coincident, showing that the intra- and extra-cube bonds are composed of distinct electronic states. The H^{cube}−H^{int} COHP shows a single large peak, indicative of a strong bonding interaction, so these interactions are important in determining structure. By comparing to the MOs in Figure 3 we can assign the peaks in the cube edge COHP. The a_{1g} and t_{1u} peaks are bonding and fully occupied, while the t_{2g} antibonding peak crosses the Fermi level, supporting our molecular model of $[H_8]^{3-}$ with a half-filled t_{2g} manifold. The a_{2u} peak is difficult to assign on the basis of this COHP alone, but the ambiguity can be resolved with other COHPs (see below). Corresponding plots for UH_8, in Figure S11, show very similar behaviour for the H-H and U-H COHPs; since UH_8 has no interstital H atoms, the similarity between H-H COHPs in LaH_{10} and UH_8 validates the H_8 molecule as a structural model for the periodic hydrides. One noticable difference is that the H-H t_{2g} antibonding peak is largely below E_F in UH_8, indicating greater electron transfer to the cube, as suggested above on the basis of H-H bond lengths. The right side of Figure 4 shows La-H COHPs for the cube

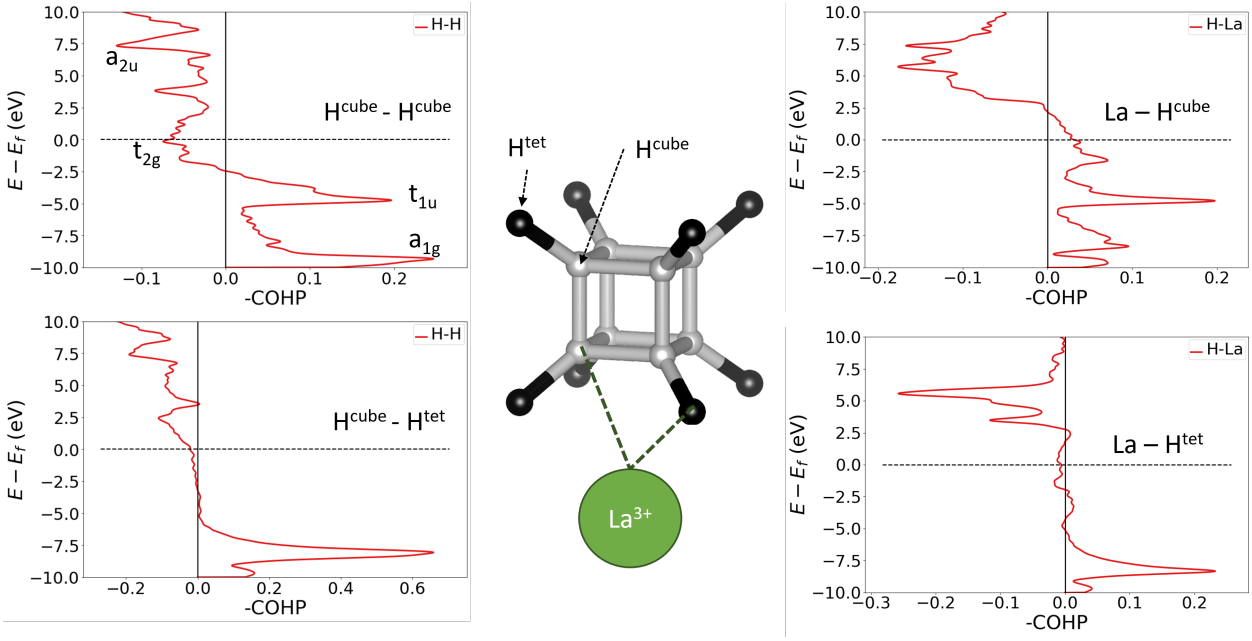

Figure 4: Crystal orbital hamilton population (COHP) analysis of LaH_{10}. H^{cube} atoms are shown in grey and H^{tet} in black. Upper left: H^{cube}−H^{cube} with annotations showing the assignment of $[H_8]$ molecular orbitals to COHP peaks. Lower left: H^{cube}−H^{tet}. Upper right: La−H^{cube}. Lower right: La−H^{tet}.

and interstitial H sites. The largest bonding peak in the La−H^{cube} COHP coincides with the t_{1u} H-H band, and the H-H t_{2g} band also coincides with an La-H bonding band that crosses the Fermi level. The interaction between H_8 t_{2g} and La $5d$ orbitals may therefore control the transport properties of LaH_{10}, possibly including superconductivity. The La−H^{tet} COHP has a single bonding peak coincident with the cube-interstitial H-H bonding peak, and an antibonding peak well above the Fermi level.

Finally, we plotted H-H COHPs for the face and body diagonals of the cube (Figure S12) - it is these plots which allow us to unambiguously assign the high-energy peak corresponding to the fully antibonding a_{2u} orbital. The peaks appear at the same energies as in the H^{cube}−H^{cube} COHP (Figure 4) but differ in their sign, *i.e.* whether they are bonding or antibonding, and the absolute values are much smaller because these are not nearest-neighbour interactions. The face diagonal behaves as expected from the MOs - the a_{1g} and a_{2u} peaks are bonding, while the t_{1u} and t_{2g} peaks are antibonding. However, the body diagonal peaks all have the opposite signs to those expected from the MOs, with a_{1g} and t_{2g} paradoxically antibonding while t_{1u} and a_{2u} are bonding. We believe that this anomaly is resolved by the fact that the H atoms at opposite corners of the cube can interact with their periodic images through a metal atom, and this interaction could be comparable in strength to the intra-cube covalency. This theory is supported by the fact that the t_{1u} peak, which overlaps strongly with the metal, is larger than the a_{1g} peak, and that the same behaviour is observed in LaH_{10} and UH_8. In conclusion, the COHP results clearly demonstrate that the H networks of the periodic materials are well represented by a molecular H_8 model.

In EuH_9 the cubes distort to a D_{2d} geometry in which four parallel edges shorten relative to the other eight (1.183 Å vs 1.214 Å at 150 GPa), and the angles distort so the faces go from square to rhombic.[24] Figure 3 shows that this is consistent with the assignment of a 2- charge to H_8.[48] Again, the orbital energies and shapes are computed by DFT but shown in a simplified representation here, and the computed results are shown in Figure S10. Placing two electrons in the t_{2g} orbitals renders the structure unstable with respect to

a Jahn-Teller distortion which lowers the symmetry to stabilize that pair of electrons. The reduction in symmetry causes the triply degenerate t_{2g} to separate into a b_2 orbital and a doubly degenerate e pair. The occupied $2b_2$ orbital is bonding along four edges of the cluster and antibonding along the other eight, consistent with the observed distortion. Oxidation state and MO analysis therefore successfully explains the H_8 cube distortion observed only in EuH_9, and this distortion, which makes the tetrahedral sites inequivalent, may be the reason that a cubic EuH_{10} phase has not been observed.[24]

Conclusions

Structural trends in the high-pressure hydrides UH_8, EuH_9, and LaH_{10} have been rationalised by the intuitive chemical tools of oxidation states and molecular orbital theory. Viewing the hydrogen networks as an assemblage of atoms and clusters, rather than a metal-centered clathrate, allows us to divide the H atoms into chemically meaningful groups and study their electronic structures. *Ab initio* atomic charge calculations, using the QTAIM and Mulliken formalisms, show that some H atoms are effectively neutral in the lattice, while the H_8 cubes are anionic. Formal oxidation states for the metals were assigned on the basis of charge calculations, so the electronic structures of the hydrides could be discussed in terms of electron transfer from metal atoms to hydrogen clusters. Molecular orbital descriptions of the H_8 clusters, validated by COHP analysis, rationalize the observed crystal structures, including a Jahn-Teller distortion in EuH_9. These methods can be easily applied to predictions of composition and structure in the growing family of compressed metal hydrides.

Acknowledgement

The authors acknowledge computational resources from the National Energy Research Scientific Computing Center (NERSC), a U.S. Department of Energy Office of Science User Facility located at Lawrence Berkeley National Laboratory, and DOE-BES grant DE-SC0019152.

Supporting Information Available

Method testing results and additional electronic structure figures (PDF), and geometries of all optimized structures in VASP POSCAR format (zip archive).

References

(1) Ashcroft, N. W. Metallic hydrogen - a high-temperature superconductor. *Physical Review Letters* **1968**, *21*, 1748.

(2) Drozdov, A. P.; Eremets, M. I.; Troyan, I. A.; Ksenofontov, V.; Shylin, S. I. Conventional superconductivity at 203 kelvin at high pressures in the sulfur hydride system. *Nature* **2015**, *525*, 73–+.

(3) Wang, H.; Tse, J. S.; Tanaka, K.; Iitaka, T.; Ma, Y. M. Superconductive sodalite-like clathrate calcium hydride at high pressures. *Proceedings of the National Academy of Sciences of the United States of America* **2012**, *109*, 6463–6466.

(4) Ma, L.; Wang, K.; Xie, Y.; Yang, X.; Wang, Y. Y.; Zhou, M.; Liu, H. Y.; Yu, X. H.; Zhao, Y. S.; Wang, H. B.; Liu, G. T.; Ma, Y. M. High-Temperature Superconducting Phase in Clathrate Calcium Hydride CaH_6 up to 215 K at a Pressure of 172 GPa. *Physical Review Letters* **2022**, *128*.

(5) Drozdov, A. P.; Kong, P. P.; Minkov, V. S.; Besedin, S. P.; Kuzovnikov, M. A.; Mozaffari, S.; Balicas, L.; Balakirev, F. F.; Graf, D. E.; Prakapenka, V. B.; Greenberg, E.; Knyazev, D. A.; Tkacz, M.; Eremets, M. I. Superconductivity at 250 K in lanthanum hydride under high pressures. *Nature* **2019**, *569*, 528–+.

(6) Snider, E.; Dasenbrock-Gammon, N.; McBride, R.; Wang, X. Y.; Meyers, N.; Lawler, K. V.; Zurek, E.; Salamat, A.; Dias, R. P. Synthesis of Yttrium Superhydride

Superconductor with a Transition Temperature up to 262 K by Catalytic Hydrogenation at High Pressures. *Physical Review Letters* **2021**, *126*.

(7) Snider, E.; Dasenbrock-Gammon, N.; McBride, R.; Debessai, M.; Vindana, H.; Vencatasamy, K.; Lawler, K. V.; Salamat, A.; Dias, R. P. Room-temperature superconductivity in a carbonaceous sulfur hydride. *Nature* **2020**, *586*, 373–+.

(8) van der Marel, D.; Hirsch, J. E. Room-temperature superconductivity - or not? Comment on Nature 586, 373 (2020) by E. Snider et al. *International Journal of Modern Physics B*

(9) Hirsch, J. E. Superconducting materials: Judge and jury of BCS-electron-phonon theory. *Applied Physics Letters* **2022**, *121*.

(10) Hirsch, J. E. Hole superconductivity xOr hot hydride superconductivity. *Journal of Applied Physics* **2021**, *130*.

(11) Novakovic, L.; Sayre, D.; Schacher, D.; Dias, R. P.; Salamat, A.; Lawler, K. V. Dispersion interactions in proposed covalent superhydride superconductors. *Physical Review B* **2022**, *105*.

(12) Woodley, S. M.; Catlow, R. Crystal structure prediction from first principles. *Nature Materials* **2008**, *7*, 937–946.

(13) Hilleke, K. P.; Zurek, E. Tuning chemical precompression: Theoretical design and crystal chemistry of novel hydrides in the quest for warm and light superconductivity at ambient pressures. *Journal of Applied Physics* **2022**, *131*.

(14) Miao, M. S.; Sun, Y. H.; Zurek, E.; Lin, H. Q. Chemistry under high pressure. *Nature Reviews Chemistry* **2020**, *4*, 508–527.

(15) Falls, Z.; Avery, P.; Wang, X. Y.; Hilleke, K. P.; Zurek, E. The XtalOpt Evolutionary

Algorithm for Crystal Structure Prediction. *Journal of Physical Chemistry C* **2021**, *125*, 1601–1620.

(16) Oganov, A. R.; Pickard, C. J.; Zhu, Q.; Needs, R. J. Structure prediction drives materials discovery. *Nature Reviews Materials* **2019**, *4*, 331–348.

(17) Wang, Y. C.; Lv, J.; Gao, P. Y.; Ma, Y. M. Crystal Structure Prediction via Efficient Sampling of the Potential Energy Surface. *Accounts of Chemical Research* **2022**, *55*, 2068–2076.

(18) Liu, H. Y.; Naumov, I.; Hoffmann, R.; Ashcroft, N. W.; Hemley, R. J. Potential high-Tc superconducting lanthanum and yttrium hydrides at high pressure. *Proceedings of the National Academy of Sciences of the United States of America* **2017**, *114*, 6990–6995.

(19) Zhang, Z. H.; Cui, T.; Hutcheon, M. J.; Shipley, A. M.; Song, H.; Du, M. Y.; Kresin, V. Z.; Duan, D. F.; Pickard, C. J.; Yao, Y. S. Design Principles for High-Temperature Superconductors with a Hydrogen-Based Alloy Backbone at Moderate Pressure. *Physical Review Letters* **2022**, *128*.

(20) Koshoji, R.; Kawamura, M.; Fukuda, M.; Ozaki, T. Diverse densest binary sphere packings and phase diagram. *Physical Review E* **2021**, *103*.

(21) Hopkins, A. B.; Stillinger, F. H.; Torquato, S. Densest binary sphere packings. *Physical Review E* **2012**, *85*.

(22) Hilleke, K. P.; Zurek, E. Rational Design of Superconducting Metal Hydrides via Chemical Pressure Tuning. *Angewandte Chemie-International Edition* **2022**, *61*.

(23) Fredrickson, D. C. DFT-Chemical Pressure Analysis: Visualizing the Role of Atomic Size in Shaping the Structures of Inorganic Materials. *Journal of the American Chemical Society* **2012**, *134*, 5991–5999.

(24) Semenok, D. V.; Zhou, D.; Kvashnin, A. G.; Huang, X. L.; Galasso, M.; Kruglov, I. A.; Ivanova, A. G.; Gavriliuk, A. G.; Chen, W. H.; Tkachenko, N. V.; Boldyrev, A. I.; Troyan, I.; Oganov, A. R.; Cui, T. Novel Strongly Correlated Europium Superhydrides. *Journal of Physical Chemistry Letters* **2021**, *12*, 32–40.

(25) Yi, S.; Wang, C. Z.; Jeon, H.; Cho, J. H. Stability and bonding nature of clathrate H cages in a near-room-temperature superconductor LaH_{10}. *Physical Review Materials* **2021**, *5*.

(26) Walsh, A.; Sokol, A. A.; Buckeridge, J.; Scanlon, D. O.; Catlow, C. R. A. Electron Counting in Solids: Oxidation States, Partial Charges, and Ionicity. *Journal of Physical Chemistry Letters* **2017**, *8*, 2074–2075.

(27) Nesper, R. The Zintl-Klemm Concept - A Historical Survey. *Zeitschrift Fur Anorganische Und Allgemeine Chemie* **2014**, *640*, 2639–2648.

(28) Yannello, V. J.; Fredrickson, D. C. Generality of the 18-n Rule: Intermetallic Structural Chemistry Explained through Isolobal Analogies to Transition Metal Complexes. *Inorganic Chemistry* **2015**, *54*, 11385–11398.

(29) Johnson, R. W.; Daane, A. H. Electron requirements of bonds in metal borides. *Journal of Chemical Physics* **1963**, *38*, 425.

(30) Wade, K. Structural significance of number of skeletal bonding electron-pairs in carboranes, higher boranes and borane anions, and various transition-metal carbonyl cluster compounds. *Journal of the Chemical Society D-Chemical Communications* **1971**, 792.

(31) Mingos, D. M. P. General theory for cluster and ring compounds of main group and transition elements. *Nature-Physical Science* **1972**, *236*, 99–+.

(32) Morgan, H. W. T.; Alexandrova, A. N. Electron Counting and High-Pressure Phase Transformations in Metal Hexaborides. *Inorganic Chemistry* **2022**,

(33) Guigue, B.; Marizy, A.; Loubeyre, P. Synthesis of UH7 and UH8 superhydrides: Additive-volume alloys of uranium and atomic metal hydrogen down to 35 GPa. *Physical Review B* **2020**, *102*.

(34) Kruglov, I. A.; Kvashnin, A. G.; Goncharov, A. F.; Oganov, A. R.; Lobanov, S. S.; Holtgrewe, N.; Jiang, S.; Prakapenka, V. B.; Greenberg, E.; Yanilkin, A. V. Uranium polyhydrides at moderate pressures: Prediction, synthesis, and expected superconductivity. *Science Advances* **2018**, *4*.

(35) Dronskowski, R.; Blochl, P. E. Crystal orbital Hamiltonian populations (COHP) - Energy-resolved visualization of chemical bonding in solids based on density-functional calculations. *Journal of Physical Chemistry* **1993**, *97*, 8617–8624.

(36) Deringer, V. L.; Tchougreeff, A. L.; Dronskowski, R. Crystal Orbital Hamilton Population (COHP) Analysis As Projected from Plane-Wave Basis Sets. *Journal of Physical Chemistry A* **2011**, *115*, 5461–5466.

(37) Kresse, G.; Furthmuller, J. Efficient iterative schemes for ab initio total-energy calculations using a plane-wave basis set. *Physical Review B* **1996**, *54*, 11169–11186.

(38) Blochl, P. E. Projector augmented wave method. *Physical Review B* **1994**, *50*, 17953–17979.

(39) Perdew, J. P.; Burke, K.; Ernzerhof, M. Generalized gradient approximation made simple. *Physical Review Letters* **1996**, *77*, 3865–3868.

(40) Bader, R. F. W. A quantum theory of molecular structure and its applications. *Chemical Reviews* **1991**, *91*, 893–928.

(41) Tang, W.; Sanville, E.; Henkelman, G. A grid-based Bader analysis algorithm without lattice bias. *Journal of Physics-Condensed Matter* **2009**, *21*.

(42) Maintz, S.; Deringer, V. L.; Tchougreeff, A. L.; Dronskowski, R. LOBSTER: A Tool to Extract Chemical Bonding from Plane-Wave Based DFT. *Journal of Computational Chemistry* **2016**, *37*, 1030–1035.

(43) George, J.; Petretto, G.; Naik, A.; Esters, M.; Jackson, A. J.; Nelson, R.; Dronskowski, R.; Rignanese, G. M.; Hautier, G. Automated Bonding Analysis with Crystal Orbital Hamilton Populations. *Chempluschem*

(44) Neese, F. The ORCA program system. *Wiley Interdisciplinary Reviews-Computational Molecular Science* **2012**, *2*, 73–78.

(45) Weigend, F.; Ahlrichs, R. Balanced basis sets of split valence, triple zeta valence and quadruple zeta valence quality for H to Rn: Design and assessment of accuracy. *Physical Chemistry Chemical Physics* **2005**, *7*, 3297–3305.

(46) Cossi, M.; Rega, N.; Scalmani, G.; Barone, V. Energies, structures, and electronic properties of molecules in solution with the C-PCM solvation model. *Journal of Computational Chemistry* **2003**, *24*, 669–681.

(47) Mulliken, R. S. Electronic population analysis on LCAO-MO molecular wave functions. 3. Effects of hybridization on overlap and gross AO populations. *Journal of Chemical Physics* **1955**, *23*, 2338–2342.

(48) Walsh, A. D. The electronic orbitals, shapes, and spectra of polyatomic molecules. 1. AH_2 molecules. *Journal of the Chemical Society* **1953**, 2260–2266.

TOC Graphic

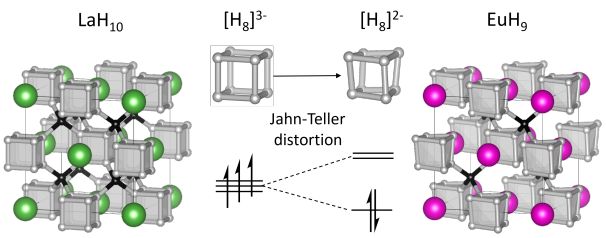

The superconducting hydrides LaH_{10}, EuH_9 and UH_8 are studied using DFT-based periodic and molecular bonding analysis. Charge calculations allow assignment of formal oxidation states and reveal that some hydrogen environments are anionic while others are neutral. A cluster model of an H_8 cube rationalises the symmetric structures of LaH_{10} and UH_8, and predicts a Jahn-Teller distortion which is observed in EuH_9. This method contributes a new dimension to explorations of high-pressure hydride chemistry.